This change in the tunneling mechanism is especially evident in the change in the Arrhenius activation energy, defined by $E_a = -Rd\ln k/d(1/T)$, where R is the gas constant and k is the rate constant. E_a increases from a negligible 0.3 J mol^{-1} at 8 K to 0.45, 1.2, and 23.6 kJ mol^{-1} at 30, 40, and 150 K, respectively. The vanishing of the activation energy at low temperatures (i.e., in the region of near-zero slope in Fig. 2) is a dramatic consequence of tunneling from only the $v = 0$ vibrational level.

At 216 K, the nontunneling ("over-barrier") component of the rate becomes equal to the tunneling ("through-barrier") contribution, and at 298 K the over-barrier component is 2.7 times larger than the through-barrier contribution. Above room temperature, E_a increases only slowly, from 25.5 kJ mol^{-1} at 298 K to 26.0 kJ mol^{-1} at 400 K. Thus, in this temperature range, the experimental Arrhenius plot for the rearrangement of **2b** to **3b** should appear to be quite linear, because the small degree of curvature, caused by the temperature dependence of E_a, would probably not be detectable. Tunneling still contributes to the rate, but like passage over the barrier, tunneling is a thermally activated process in this temperature regime.

The calculated rate constants at 8 K for rearrangement of **2a** (1.4×10^4 s^{-1}) and **2b** (9.1×10^{-6} s^{-1}) are consistent with both the failure to detect chlorocarbene **2a** and the observation of rearrangement of fluorocarbene **2b** with a half-life on the order of tens of hours at this temperature. Because theory predicts that raising the temperature from 8 to 16 K will produce a negligible change in rate, the observed increases in the rate constant for the rearrangement of **2b** to **3b** are interpreted as environmental effects on the carbene lifetime. In particular, ring expansion may be inhibited by the rigidity of the matrix, so that matrix softening could be responsible for this temperature dependence. Matrix softening would also explain the need to increase the temperature to 16 K, in order for the less reactive conformer *endo*-**2b** to rearrange in N$_2$, presumably by first isomerizing, by tunneling, to the more reactive conformer *exo*-**2b** (*30*). The greater reactivity of both conformers in Ar than in N$_2$ and the smaller temperature dependence of the rate of rearrangement in Ar are consistent with the expectation that Ar should be the softer matrix.

The dominance of tunneling in the rearrangement of **2** to **3** at low temperatures suggests that heavy-atom tunneling may be more facile than is generally recognized. In addition, the direct observation of the rearrangement of **2b** to **3b** at the low-temperature limit for this reaction suggests new possibilities for understanding, controlling, and tuning chemical reactivity at the single–quantum-state level of resolution.

References and Notes
1. B. C. Garrett *et al.*, *J. Am. Chem. Soc.* **108**, 3515 (1986).
2. D. G. Truhlar *et al.*, *Acc. Chem. Res.* **35**, 341 (2002).
3. A. Kohen, J. P. Klinman, *Chem. Biol.* **6**, R191 (1999).
4. D. J. Miller, R. Subramanian, W. H. Saunders Jr., *J. Am. Chem. Soc.* **103**, 3519 (1981).
5. B. K. Carpenter, *J. Am. Chem. Soc.* **105**, 1700 (1983).
6. A. M. Orendt *et al.*, *J. Am. Chem. Soc.* **110**, 2648 (1988).
7. R. Lefebvre, N. Moiseyev, *J. Am. Chem. Soc.* **112**, 5052 (1990).
8. B. R. Arnold, J. G. Radziszewski, A. Campion, S. S. Perry, J. Michl, *J. Am. Chem. Soc.* **113**, 692 (1991).
9. S. L. Buchwalter, G. L. Closs, *J. Am. Chem. Soc.* **101**, 4688 (1979).
10. M. B. Sponsler, R. Jain, F. D. Coms, D. A. Dougherty, *J. Am. Chem. Soc.* **111**, 2240 (1989).
11. W. Sander, G. Bucher, F. Reichel, D. Cremer, *J. Am. Chem. Soc.* **113**, 5311 (1991).
12. T. V. Albu *et al.*, *J. Phys. Chem. A* **106**, 5323 (2002).
13. R. A. Moss, G. J. Ho, W. Liu, *J. Am. Chem. Soc.* **114**, 959 (1992).
14. G. J. Ho *et al.*, *J. Am. Chem. Soc.* **111**, 6875 (1989).
15. V. I. Goldanskii, M. D. Frank-Kamenetskii, I. M. Barkalov, *Science* **182**, 1344 (1973).
16. K. Toriyama, K. Numone, M. Iwaski, *J. Am. Chem. Soc.* **99**, 5823 (1977).
17. D. P. Kiryukhin, I. M. Barkalov, V. I. Goldanskii, *J. Chem. Phys.* **76**, 1013 (1979).
18. G. C. Hancock, C. A. Mead, D. G. Truhlar, A. J. C. Varandas, *J. Chem. Phys.* **91**, 3492 (1989).
19. S. E. Wonchoba, W.-P. Hu, D. G. Truhlar, *Phys. Rev. B* **51**, 9985 (1995).
20. N. Balakrishnan, A. Dalgarno, *Chem. Phys. Lett.* **341**, 652 (2001).
21. W. J. Graham, *J. Am. Chem. Soc.* **87**, 4396 (1965).
22. P. Rempala, R. S. Sheridan, *J. Chem. Soc. Perkin Trans.* **2**, *2257* (1999).
23. Materials and methods are available as supporting material on *Science* Online.
24. R. A. Moss *et al.*, *J. Am. Chem. Soc.* **107**, 2743 (1985).
25. D. G. Truhlar, M. S. Gordon, *Science* **249**, 491 (1990).
26. B. J. Lynch, P. L. Fast, M. Harris, D. G. Truhlar, *J. Phys. Chem. A* **104**, 4811 (2000).
27. W. J. Hehre, L. Radom, P. v. R. Schleyer, J. A. Pople, *Ab Initio Molecular Orbital Theory* (Wiley, New York, 1986).
28. D. G. Truhlar, B. C. Garrett, *Annu. Rev. Phys. Chem.* **35**, 159 (1984).
29. Y.-P. Liu *et al.*, *J. Am. Chem. Soc.* **115**, 2408 (1993).
30. The CVT/SCT rate constant for this isomerization reaction at 8 to 16 K is computed to be 2.6×10^{-4} s^{-1} and is essentially the rate constant for tunneling. This value is about a factor of 10 larger than the rate of disappearance of the less reactive conformer at 8 K, even in an Ar matrix. However, the calculated rate constant is only a factor of 4 larger than the rate constant for disappearance of this isomer at 16 K in an N$_2$ matrix, where some matrix softening presumably occurs.
31. We thank NSF for support of this research at the Universities of Nevada (Reno), Minnesota, and Washington. P.S.Z. and R.S.S. also acknowledge the Donors of the American Chemical Society Petroleum Research Fund for partial support of this research.

Atomic-Resolution Imaging of Oxygen in Perovskite Ceramics

C. L. Jia, M. Lentzen, K. Urban*

Using an imaging mode based on the adjustment of a negative value of the spherical-aberration coefficient of the objective lens of a transmission electron microscope, we successfully imaged all types of atomic columns in the dielectric SrTiO$_3$ and the superconductor YBa$_2$Cu$_3$O$_7$. In particular, we were able to view the oxygen atoms which, due to their low scattering power, were not previously accessible, and this allowed us to detect local nonstoichiometries or the degree of oxygen-vacancy ordering. This technique offers interesting opportunities for research into oxides, minerals, and ceramics. In particular, this holds for the huge group of perovskite-derived electroceramic materials in which the local oxygen content sensitively controls the electronic properties.

Thin films of Ba- and Sr-based perovskites have great potential for application, in particular as high-permittivity dielectrics in microelectronics or nonvolatile memory devices. Research on the structure and properties of these materials has shown that variations in chemical composition in the bulk or in connection with lattice defects are detrimental to materials properties and device performance (*1*, *2*). Above all, it is the local oxygen content which reacts sensitively to cation disorder or lattice strain. The same applies to the cuprate high-temperature superconductors. In their perovskite-derived structure, the oxygen occupancy of certain lattice sites sensitively controls the charge carrier density in the superconducting planes (*3*, *4*).

The microstructure of perovskites can be studied by means of high-resolution transmission electron microscopy (HRTEM). Under suitable conditions it is possible to image the cation columns projected along the viewing direction. Because the cations have a high nuclear charge, their scattering power is high, resulting in strong phase contrast. In comparison, due to the relatively low scattering power, it is difficult to image the oxygen sublat-

Institute of Solid State Research, Research Center Juelich, D-52425 Juelich, Germany.

*To whom correspondence should be addressed. E-mail: k.urban@fz-juelich.de

tice. The conditions under which oxygen gives rise to detectable contrast in the high-temperature superconductor $YBa_2Cu_3O_7$ were studied by quantum-mechanical and wave-optical image computer simulation (5–8). It was found that, in conventional HRTEM, weak phase contrast could be expected from the oxygen sublattice, although only under very special imaging conditions. Indeed, long-range superlattice ordering of oxygen vacancies in $YBa_2Cu_3O_7$ has been detected experimentally (5, 7–9). Importantly, in this earlier HRTEM work atomic resolution could not be achieved. Rather, the presence of oxygen was deduced from the intensity of broad modulated bands of contrast also acting as "fingerprints" for oxygen-vacancy ordering. The intensity distribution of these bands is controlled not only by oxygen but also by copper, and their width is determined by the long-range Fourier components of the crystal potential. Because, on account of the limited resolution, higher-order Fourier components are missing, these images do not provide information on the atomic scale. Information on individual oxygen atom columns was obtained by the focus-variation technique, in which the electron wave function at the exit plane of the specimen is calculated by computer processing of a series of typically 20 images recorded as the objective lens focal length is varied (10, 11). Individual oxygen columns could be resolved in unprocessed images of ZrO_2 but not of $YBa_2Cu_3O_7$ with a high-voltage electron microscope operated at the high electron energy of 1 MeV, which introduces radiation damage into the specimen (12). Difficulties in imaging oxygen arise not only in phase-contrast HRTEM but also in the high-angle annular dark-field technique in the scanning transmission electron microscope (13). This technique has been successfully used to image Sb atoms in Si and Au on carbon (14, 15). However, in a recent study on $SrTiO_3$ and $LaTiO_3$ superlattices, only the cation sublattice could be imaged (16).

We used a transmission electron microscope (TEM) with a field-emission gun operated at an accelerating voltage of 200 kV. It is equipped with an electromagnetic hexapole system, which allows for the correction of the spherical aberration of the objective lens (17). As measured by the Young's fringe technique this instrument offers, with respect to its transfer function, an information limit better than 0.13 nm, corresponding to 7.7 nm^{-1} in reciprocal space (18). A comparison with the atomic distances occurring in the projection of $SrTiO_3$ along the crystallographic [011] direction indicates that this should be sufficient to resolve all the atom positions in the compound, including those of oxygen, provided that there is sufficient contrast.

The basis of phase contrast is the locally variable phase shift of the electron waves by the interatomic potential (19, 20). As long as this phase shift is small—i.e., in ideally thin or "weak" objects—the resulting electron wave function can be described by a transmitted beam and low-amplitude diffracted beams phase shifted by $\pi/2$. To convert phase into amplitude information, the only form in which it can be registered on film or by a charge-coupled device (CCD) camera, an additional phase shift is required. This is achieved by exploiting the phase shifts introduced by the spherical aberration and by the defocus aberration of the objective lens. In a conventional TEM the spherical aberration coefficient C_S is a fixed parameter causing a specific, unavoidable phase shift. Therefore, the objective lens is adjusted for a small deviation ΔZ from Gaussian focus to deliberately produce an additional phase shift which, together with that induced by the spherical aberration, yields a value as close as possible to $\pi/2$ over the whole spatial-frequency spectrum required to properly image the atomic structure. As a result, the overall phase shift of the diffracted beams is close to π, their amplitude is subtracted from that of the transmitted beam, and in the image the atoms appear dark on a light background.

We find that the aberration-correction system in our microscope, initially designed to compensate the original $C_S = 1.23$ mm to zero, offers the great advantage that, by proper excitation of the hexapoles, C_S can be continuously adjusted within wide limits. This means that we have two parameters, ΔZ and C_S, available to tune the microscope for optimum contrast. The optimization problem resulting from the fact that increasing C_S improves contrast, but at the cost of resolution, can be solved by equating the expression for the value of Scherzer's defocus to that of Lichte's defocus of least confusion (18). We find that compensating the aberration not to zero but to the small residual value of 40 μm and combining this with an underfocus of $\Delta Z = -8$ nm should result in good contrast up to the information limit of the microscope. The progress achieved in this way is demonstrated by the calculated images displayed in Fig. 1. The strongly blurred and inadequate image obtained from $SrTiO_3$

without aberration correction is shown in (B). The image obtained under the new conditions is shown in (C). The strontium atoms exhibit strong contrast, and in between the atoms a horizontal dark band occurs at the position of the titanium-oxygen atom rows.

Exploiting the excitation range of the hexapoles even further, we find that we can overcompensate the objective-lens aberration, resulting in negative C_S values. The intriguing result is that by combining this negative value with the adjustment of an overfocus, the contrast not only becomes inverted—i.e., atoms appear bright on a dark background—but it also increases steeply. In Fig. 1D, calculated with $C_S = -40$ μm and $\Delta Z = +8$ nm, the atomic images are very sharp and oxygen can be seen well separated from titanium. That this imaging condition provides us with real atomic resolution can be tested by calculating images for which the occupancy of a single atomic column of oxygen is set to 0% (Fig. 1E) and to 50% (Fig. 1F). The effect of displacing the column by 0.05 nm along the [100] direction is shown in Fig. 1G. From the image it is apparent that the change in contrast is restricted to the selected atomic column. The contrast is rather robust with respect to a variation of the imaging conditions. The sample thickness can vary between 2.5 and 5 nm and the defocus value between 7 and 12 nm without seriously changing the contrast.

We investigated the negative-C_S imaging mode by quantum-mechanical and wave-optical image simulation using the MacTempas software package (21). The contrast inversion can be understood within the linear imaging theory of weak objects. Phase-shifting the diffracted beams by $-\pi/2$ means that their amplitude is added to that of the transmitted beam, resulting in bright atom images. On the other hand, the dramatic sharpening of the atom contrast leading to the observed increase of the effective image resolution is only obtained on the basis of the full quantum-mechanical nonlinear multibeam treatment (Fig. 1D), whose intricate phase relations do not lend themselves to a simple interpretation. To test the generality

Fig. 1. Calculated images of $SrTiO_3$, demonstrating the improvement in image resolution. (**A**) Structure projected along the [011] crystal direction. (**B**) Image under Scherzer focus conditions in the uncorrected instrument; $C_S = 1.23$ mm, $\Delta Z = -68$ nm. (**C**) Image for $C_S = +40$ μm and $\Delta Z = -8$ nm. (**D**) Image for the new imaging mode, adjusting for $C_S = -40$ μm and $\Delta Z = +8$ nm. The calculations here are carried out for a specimen 4 nm thick. The attainment of real atomic resolution is demonstrated by calculations for (**E**) an empty oxygen column, (**F**) a 50% oxygen occupancy, and (**G**) a shift of the oxygen column by 0.05 nm. The effect on contrast is localized at the single atomic column (arrow).
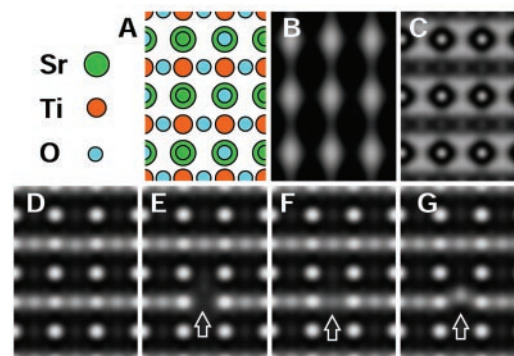
of the negative-C_S imaging mode, we carried out image calculations for a number of materials, among them Si and Ge [011], for positive and negative spherical aberration. In all cases, the contrast improvement obtained with negative C_S and the gain for the direct structure interpretation is striking. The calculations show that the nonlinear contrast contributions diminish the image contrast relative to the linear image for the positive-C_S setting, whereas they reinforce the image contrast relative to the linear image for the negative-C_S setting.

Figure 2 shows an experimental image of $SrTiO_3$ [011] for $C_S = -40$ μm and $\Delta Z = +8$ nm (22). It demonstrates the high quality of the

images and that the oxygen-atom columns can be seen and studied individually. At positions 1 and 2, the oxygen-atom contrast is weaker than in the neighboring oxygen positions. This is shown quantitatively by the intensity trace (23) in inset (A). The calculated image in inset (B), evaluated quantitatively in inset (C), perfectly matches the experimental data, indicating that the occupancy of the oxygen columns at position 1 is only 85% and at position 2 it is 80% of the stoichiometric value. Our image simulations show that there is a lower limit of oxygen detection corresponding to about 30% column occupancy.

Figure 3 shows the application of the nega-

tive-C_S imaging mode to $YBa_2Cu_3O_7$. In (A) a 90° tilt boundary (black arrow) is shown where the crystal orientation (parallel to the viewing direction) changes from [100] in the upper part to [001] in the lower part of the image. Comparison with the structure model (C) indicates that, in addition to the cations Ba, Y, and Cu, we image oxygen at atomic resolution in the Cu-O–chain planes (one of them marked by red arrow), in the CuO_2 planes (above and below the Y atom), and in the BaO planes. Dark contrast on both sides of the Y atom supports the absence of oxygen, in agreement with the structure model. In the lower part of Fig. 3A, below the tilt boundary, we see end-on the oxygen-atom columns extending along the [001] direction, well separated from the copper-oxygen columns. Information on oxygen-vacancy ordering can be obtained by inspection of Fig. 3B and a comparison of the atom contrast in the Cu-O–chain planes with that in the upper part of Fig. 3A. Because these two images are tilted by 90° around a vertical axis with respect to each other, the horizontal atom rows of (A) are seen end-on in (B). We recognize that in (B), in the Cu-O–chain planes (red arrow), the atom positions between the Cu atoms are empty, whereas they are occupied by oxygen in (A). This provides evidence of a high degree of oxygen ordering in these planes based on -Cu-O-Cu-O-Cu-O- atom sequences along [010] and -Cu-V-Cu-V-Cu-V- sequences along [100], where V denotes vacant oxygen sites.

In both Fig. 3, A and B, a stacking fault also occurs, as indicated by two red horizontal arrowheads. The two images were taken at different locations of the sample. They are, however, arranged in such a way that it becomes evident that they represent two views, tilted by 90° with respect to the vertical axis, of the same type of fault. The shift by one half of the [010] lattice parameter in Fig. 3A and the occurrence of a Cu-O double layer in (B) indicates a so-called "124" fault because periodic arrangements of such faults occur in the structure of $YBa_2Cu_4O_8$ (10, 24). In Fig. 3B, the enhanced white contrast of the Cu-O atom columns in the fault provides evidence of a high oxygen occupancy and highly perfect ordering. This can be explained by particularly strong Cu-O bonds along the [010] direction (25). The study of such atomic detail, including both the cation and the oxygen sublattices, provides access to stoichiometric and structural defects in ferroelectric and superconducting heterostructures that have long been known to hamper their performance in microelectronic applications but until now could not be investigated in detail.
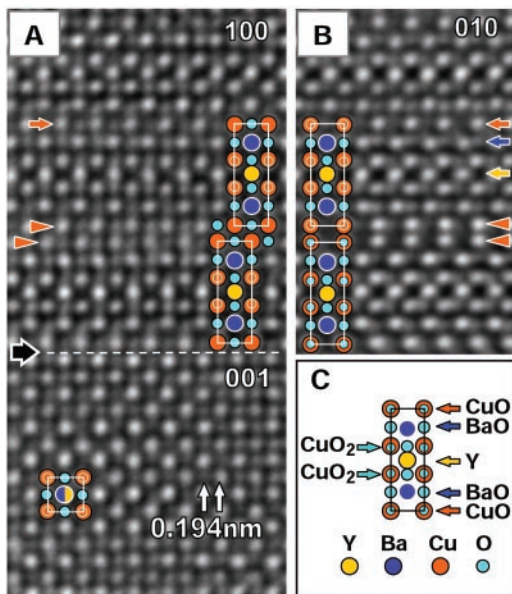

Fig. 2. Experimental image of $SrTiO_3$ [011]. The spherical aberration coefficient was adjusted for $C_S = -40$ μm, and an overfocus of $\Delta Z = +8$ nm was used. Atom columns in the ~4-nm-thick specimen appear bright on a dark background, and oxygen is atomically resolved. At positions 1 and 2 the oxygen-atom contrast is weaker than in the neighboring oxygen-atom positions. This is shown quantitatively by the intensity trace in inset (**A**). This trace was taken directly from the digital readout of the CCD camera. Inset (**B**) shows a calculated image, assuming a reduced oxygen occupancy of 85 and 80%, respectively, for the oxygen-atom columns 3 and 4. The corresponding intensity trace [inset (**C**)] is in good agreement with the experimental trace (A).
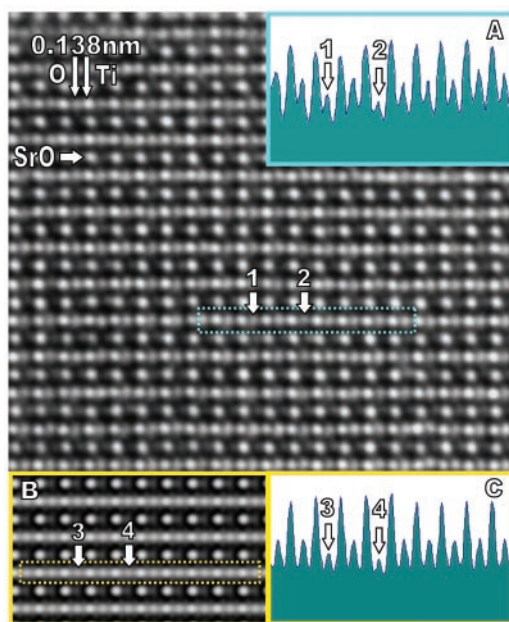
Fig. 3. Experimental images of $YBa_2Cu_3O_7$ in different crystal orientations. (**A**) A 90° tilt boundary (black arrow) separates two crystal domains. In the upper part, the crystal orientation (along the viewing direction) is parallel to [100], whereas it is parallel to [001] in the lower part of the image. Comparison with the structure model (**C**) indicates that all atomic positions of the cations Ba, Y, and Cu and of the oxygen are imaged white on a dark background at atomic resolution. In the upper part of (A), clearly alternating copper and oxygen occupancy can be seen along the horizontal [010] Cu-O chains (red arrow). (**B**) The crystal is imaged along the [010] direction—i.e., tilted with respect to (A)—by 90° around the vertical axis. The [010] Cu-O chains are now seen end-on. The potential oxygen positions in between the Cu-atom positions in the so-called Cu-O–chain planes (red arrow) are empty. This provides evidence of oxygen ordering in the Cu-O–chain planes. In (A) and (B) a "124" fault also occurs (marked by double arrowheads) seen along the [100] and [010] crystal directions, respectively. In (B), the enhanced bright contrast of the [010] Cu-O chains (seen end-on) in the fault plane indicates high oxygen occupancy and ordering there.

References and Notes
1. R. Waser, *Integr. Ferroelect.* **15**, 39 (1997).
2. A. K. Tagantsev, I. Stolichnov, E. L. Colla, N. Setter, *J. Appl. Phys.* **90**, 1397 (2001).
3. D. Jorgensen *et al.*, *Phys. Rev. B* **36**, 3608 (1987).
4. C. P. Poole, H. A. Farach, R. J. Creswick, *Superconductivity* (Academic Press, San Diego, CA, 1995).

5. A. Ourmazd, J. C. H. Spence, *Nature* **329**, 425 (1987).
6. N. P. Huxford, D. J. Eaglesham, C. J. Humphreys, *Nature* **329**, 812 (1987).
7. Y. Yan, M. G. Blanchin, *Phys. Rev.* **43**, 13717 (1991).
8. T. Krekels, G. Van Tendeloo, S. Amelinckx, *Appl. Phys. Lett.* **59**, 3048 (1991).
9. G. Van Tendeloo, T. Krekels, in *Characterization of High T_C Materials and Devices by Electron Microscopy*, N. D. Browning, S. J. Pennycook, Eds. (Cambridge Univ. Press, Cambridge, 2000), pp. 161–191.
10. W. Coene, G. Janssen, M. Op de Beeck, D. Van Dyck, *Phys. Rev. Lett.* **69**, 3743 (1992).
11. C. L. Jia, A. Thust, *Phys. Rev. Lett.* **82**, 5052 (1999).
12. S. Horiuchi *et al.*, *Ultramicroscopy* **39**, 231 (1991).
13. S. J. Pennycook, D. E. Jesson, P. D. Nellist, M. F. Chisholm, N. D. Browning, in *Handbook of Microscopy*, S. Amelinckx *et al.*, Eds. (Wiley-VCH, Weinheim, Germany, 1997), vol. 2, pp. 595–620.
14. P. M. Voyles, D. A. Muller, J. L. Grazul, P. H. Citrin, H. J. L. Gossmann, *Nature* **416**, 826 (2002).
15. P. E. Batson, N. Dellby, O. L. Krivanek, *Nature* **418**, 617 (2002).
16. A. Ohtomo, D. A. Muller, J. L. Grazul, H. Y. Hwang, *Nature* **419**, 378 (2002).
17. M. Haider *et al.*, *Nature* **392**, 768 (1998).
18. M. Lentzen *et al.*, *Ultramicroscopy* **92**, 233 (2002).
19. J. C. H. Spence, *Experimental High-Resolution Electron Microscopy* (Oxford Univ. Press, New York, 1988).
20. D. B. Williams, C. B. Carter, *Transmission Electron Microscopy* (Plenum, New York, 1996).
21. R. Kilaas, in *Proceedings of the 45th Annual Meeting of the Electron Microscopy Society of America*, Baltimore, MD, G. W. Bailey, Ed. (San Francisco Press, San Francisco, 1987), pp. 66–67.
22. All experimental images presented are prints obtained from the original and unfiltered digital CCD camera recordings.
23. Intensity traces were taken from the nonprocessed, original digital data.
24. H. W. Zandbergen, R. Gronsky, K. Wang, G. Thomas, *Nature* **331**, 596 (1988).
25. D. E. Morris *et al.*, *Phys. Rev. B* **40**, 11406 (1989).

7 October 2002; accepted 20 December 2002

Formation of Electron Holes and Particle Energization During Magnetic Reconnection

J. F. Drake,[1]* M. Swisdak,[1] C. Cattell,[2] M. A. Shay,[1] B. N. Rogers,[3] A. Zeiler[4]

Three-dimensional particle simulations of magnetic reconnection reveal the development of turbulence driven by intense electron beams that form near the magnetic x-line and separatrices. The turbulence collapses into localized three-dimensional nonlinear structures in which the electron density is depleted. The predicted structure of these electron holes compares favorably with satellite observations at Earth's magnetopause. The birth and death of these electron holes and their associated intense electric fields lead to strong electron scattering and energization, whose understanding is critical to explaining why magnetic explosions in space release energy so quickly and produce such a large number of energetic electrons.

Magnetic reconnection is the driver of explosions in laboratory, space, and astrophysical plasmas, including solar and stellar flares and storms in Earth's magnetosphere. In the classic picture of magnetic reconnection, oppositely directed components of the magnetic field cross-link, forming a magnetic x-line configuration. The expansion of the newly reconnected field lines away from the x-line releases the magnetic energy and pulls in the oppositely directed magnetic flux to sustain the energy release process. Some form of dissipation is required to allow the plasma and magnetic field to decouple so that the topological change in the magnetic field can take place. The rate of reconnection, however, is sensitive to the plasma resistivity (*1–3*) such that reconnection based on classical resistivity is orders of magnitude too slow to explain the fast release of magnetic energy observed in nature. To explain the large discrepancy between observations of energy release times and the predictions, it was postulated that the plasma resistivity is enhanced above the classical values by electron scattering associated with electric field fluctuations (*4*). These fluctuations could be driven by the intense currents that form during magnetic reconnection. The resulting anomalous resistivity fortuitously also facilitates fast reconnection, which is insensitive to resistivity (*5, 6*).

The concept of anomalous resistivity also has a secondary benefit. Observations of solar flares indicate that up to half of the energy released in magnetic reconnection is carried by energetic electrons (*7*). The direct production of very energetic electrons during magnetic reconnection in Earth's magnetotail has also been reported (*8*). The mechanism for such strong electron heating remains unclear. The flows that develop during reconnection are typically of the order of the Alfvén speed $c_A = B/[(4\pi\rho)^{1/2}]$, where B is the magnetic field strength and ρ is the plasma mass density, and are therefore too slow to produce the near relativistic electron velocities observed. The development of high-frequency turbulence, which could cause the electron scattering associated with anomalous resistivity, would also heat electrons and perhaps produce the broad spectrum of energetic electrons observed in nature.

Anomalous resistivity has been widely invoked to explain the fast release of energy observed in nature, but the concept remains poorly understood (*4*). The strongest evidence for its existence comes from observations in the auroral region of the ionosphere, where localized regions of large parallel electric field have been measured (*9, 10*). These localized structures take the form of double layers (which support a net drop in the electric potential) or electron holes (regions of depressed electron density that exhibit a bipolar parallel electric field).

We carried out three-dimensional (3D) particle simulations of magnetic reconnection to explore the self-consistent development of current-driven instabilities and anomalous resistivity and compared the results with observations from the Polar spacecraft at Earth's magnetopause. In earlier simulations of a system with a reversed field and no imposed ambient guide (out-of-plane) magnetic field, no current-driven instabilities developed around the x-line (*11*). The intrinsic electron heating around the null field region was sufficient to stabilize current-driven instabilities. In our simulations, an imposed guide field prevents the demagnetization of electrons and associated heating. The initial equilibrium is a double current layer with two magnetic field components B_x and B_z dependent on the spatial coordinate y:

$$\frac{B_x}{B_0} = \tanh\frac{y - L_y/4}{w_0} - \tanh\frac{y - 3L_y/4}{w_0} - 1$$

(1)

where B_0 is the asymptotic field strength outside of the current layers; $B_z = (B^2 - B_x^2)^{1/2}$ is chosen so that the total field B is constant. For the 3D simulations shown, the computational domain has dimensions $L_x = 4d_i$, $L_y = 2d_i$, $L_z = d_i$ and periodic boundary conditions. The scale length d_i is the ion inertial length c/ω_{pi}, where ω_{pj} is the plasma frequency of a particle species j, and $w_0 = 0.25d_i$ is the current layer thickness. The initial plasma pressure is constant with the density n_0 and electron and ion temperatures $T_e = T_i = 0.04 \, m_i c_A^2$, where $c_A = B_0/[(4\pi \, n_0 m_i)^{1/2}]$. Other parameters are B

[1]University of Maryland, College Park, MD 20742, USA. [2]School of Physics and Astronomy, University of Minnesota, Minneapolis, MN 55455, USA. [3]Department of Physics and Astronomy, Dartmouth College, Hanover, NH 03755, USA. [4]Centre for Interdisciplinary Plasma Science, Max-Planck-Institut für Plasmaphysik, 85748 Garching, Germany.

*To whom correspondence should be addressed. E-mail: drake@plasma.umd.edu